Active procedures to control the flow past the Ahmed body with a 25° rear window

Charles-Henri Bruneau*

IMB, Université Bordeaux 1, Team MC2 INRIA Bordeaux-Sud-Ouest, UMR 5251 CNRS
351 cours de la Libération, F-33405 Talence
bruneau@math.u-bordeaux1.fr *Corresponding author

Emmanuel Creusé

Laboratoire Paul Painlevé Université Lille 1, Sciences et Technologies, Team SIMPAF INRIA Lille Nord Europe, UMR 8524 CNRS, Cité Scientifique, F-59655 Villeneuve d'Ascq
creuse@math.univ-lille1.fr

Delphine Depeyras

IMB, Université Bordeaux 1, Team MC2 INRIA Bordeaux-Sud-Ouest, UMR 5251 CNRS
351 cours de la Libération, F-33405 Talence
depeyras@math.u-bordeaux1.fr

Patrick Gilliéron

Technocentre Renault, Direction de La Recherche, Mécanique des fluides et aérodynamique, DREAM/DTAA
1, Avenue du Golf F-78288 Guyancourt
patrick.gillieron@renault.com

Iraj Mortazavi

IMB, Université Bordeaux 1, Team MC2 INRIA Bordeaux-Sud-Ouest, UMR 5251 CNRS
351 cours de la Libération, F-33405 Talence
mortaz@math.u-bordeaux1.fr

Abstract: Ahmed body with a 25° rear window is used to represent a simplified car geometry. Two and three-dimensional simulations are performed to analyse the flow behaviour around such a vehicle. Sucking and blowing jets or slots are added on the body to control the flow. The results presented show that good drag reductions are achieved for a good choice of the active procedure.

Keywords: Direct numerical simulation, Active flow control, Ahmed body with a rear window.

Reference to this paper should be made as follows: Bruneau C.H., Creusé E., Depeyras D., Gilliéron P. and Mortazavi I., (xxxx) 'Active

procedures to control the flow past the Ahmed body with a 25° rear window', *Int. J. Aerodynamics*, Vol. x, No. x, pp.xxx–xxx.

Biographical notes: Charles-Henri Bruneau is professor in applied mathematics at the University of Bordeaux, France. His research interest is mainly concerned by the simulation, analysis and control of fluid dynamics.
Emmanuel Creusé is professor in applied mathematics at the University of Lille, France. His research field is devoted to numerical methods for partial differential equations approximation arising in particular in fluid dynamics.
Delphine Depeyras is doctor-engineer in a company linked to aeronautics and space.
Iraj Mortazavi is associate professor at the University of Bordeaux, France. His research is devoted to the computational fluid dynamics and the development of novel flow control techniques.
Patrick Gilliéron is a researcher, head of the research group on fluid mechanics and aerodynamics at Renault car industry. His work concerns mainly the control of the separation zones and the transient phenomena.

1 Introduction

The research developed today in car aerodynamics is carried out from the point of view of sustainable development. Some car companies have the objective to develop control solutions able to reduce the aerodynamic drag of the vehicles by at least 30% without constraints on the design, the comfort, the storage or the safety of the passengers. Thus, it is necessary to modify locally the flow, to remove or delay the separation position or to reduce the development of the recirculation zone at the back and of the separated swirling structures Gilliéron (2002).

This can be mainly obtained by controlling the flow near the wall with or without additional energy using active or passive devices Fieldler and Fernholz (1990); Gilliéron (2002). Significant results can be obtained using simple techniques Roshko and Koening (1976); Bruneau and Mortazavi (2008). In practise, the flow control is obtained when the wall pressure distribution is successfully modified on the back and on the rear window, using various adapted devices which change locally the geometry. Control experiments in wind tunnel on reduced or real ground vehicles are performed and measurements of the wall static pressures and of the aerodynamic torque allow to quantify the effect of the control Gilliéron and Chometon (1999); Cooper (1985); Gilliéron (2002); Roshko and Koening (1976); Rouméas et al. (2009). However, due to the design constraints, the real gain is rather weak and so new control techniques have to be developed. Among these new techniques in progress, separate devices located in front of or behind the vehicle can be used to reduce the development of the recirculation zone on the rear window or at the back and the interactions of the swirling wake structures.

A famous benchmark that is commonly used in the ground vehicle industry is the Ahmed body Ahmed et al. (1984). It is a three-dimensional bluff body moving

in the vicinity of the ground generating a turbulent flow. Several separations appear along the body from the front to the back. The resulting recirculation zones contribute to a significant part of the drag coefficient Gilliéron and Spohn (2002); Onorato et al. (1984). This coefficient changes strongly with the angle α between the horizontal line and the rear window (even for the two-dimensional flow). For a square back Ahmed body (without a rear window), the flow separates at the back and is mainly a two-dimensional base flow. Indeed, experimental and numerical studies confirm the two-dimensional behaviour of the detached near-wall flow at the base of the square back Ahmed body geometry Rouméas et al. (2009); Gilliéron and Chometon (1999); Krajnović and Davidson (2003); Brunn et al. (2007). On the contrary, for the angles α situated in the range of 12° to 30°, the flow is highly three-dimensional over the rear window as there are two counter-rotating lateral vortices and an open separation zone Onorato et al. (1984); Gilliéron and Chometon (1999); Rouméas et al. (2009); Lienhart et al. (2000) that yield a drag enhancement. This paper is devoted to this last case.

In this paper we focus on the active control procedure used to reduce the drag coefficient. Two and three-dimensional computations are performed to simulate the flow of an incompressible fluid at Reynolds number 30,000 based on the body length around the Ahmed body solving directly the Navier-Stokes equations. The modelling and numerical simulation are presented in the next section. Then the active control is tested on two-dimensional and three-dimensional geometries. The results are carefully analysed to show what are the mechanisms of the control.

2 Modelling and numerical simulation

2.1 Penalization method

In this section, the method used to simulate the flow past the Ahmed body on top of a road using Cartesian grids is presented. The now well-known penalization method is used to take into account the solid Ahmed body (Angot et al. (1999); Bruneau and Mortazavi (2008)). In this method a Cartesian mesh of a rectangular domain including the body is used. Among the immersed boundary methods this method has the advantage to be very easy to implement as it requires only to specify the medium parameter at each point of the discretization according to its position in the fluid or in the solid parts of the domain. Then the penalized Navier-Stokes equations for the velocity and pressure (U, p) as unknowns are solved without any specific treatment of the body or its boundary. These equations for an incompressible fluid are given by:

$$\partial_t U + (U \cdot \nabla)U - \frac{1}{Re}\Delta U + \frac{U}{K} + \nabla p = 0 \; in \; \Omega_T = \Omega \times (0, T) \tag{1}$$

$$\nabla \cdot U = 0 \; in \; \Omega_T \tag{2}$$

where Re is the Reynolds number based on the height H of the Ahmed body, the mean velocity u_∞ at the entrance section and the kinematic viscosity ν of the fluid. K is the non dimensional coefficient of permeability of the medium and Ω is the full domain including the porous layer and the solid body. In the

fluid the permeability coefficient goes to infinity, the penalization term vanishes and we solve the non dimensional Navier-Stokes equations. In the solid body the permeability coefficient goes to zero and it has been shown in Angot et al. (1999) that solving these equations corresponds to solve Darcy's law in the solid and that the velocity is proportional to K. For numerical simulations we set $K = 10^{16}$ in the fluid and $K = 10^{-8}$ in the solid body. The equations (1), (2) above are associated to an initial datum ($X = (x, y, z)$):

$U(X, 0) = U_0(X)$ *in* Ω

and the following boundary conditions (see Figure 4):

$U = U_\infty = (u_\infty, 0, 0) = (1, 0, 0)$ on the entrance section Γ_D and on the road Γ_0;

$\sigma(U, p)n + \frac{1}{2}(U \cdot n)^-(U - U_{ref}) = \sigma(U_{ref}, p_{ref})n$ on the open boundaries Γ_N

to convey properly the vortices through the artificial frontiers Bruneau and Fabrie (1994), where $\sigma(U, p) = 1/Re(\nabla U + \nabla U^t) - pI$ is the stress tensor, (U_{ref}, p_{ref}) a reference state, n is the unit normal pointing outside of the domain and the notation $a = a^+ - a^-$ is used.

Then a simulation is performed using a second-order Gear scheme in time with explicit treatment of the convection term, for which the space discretization is based on a third-order finite differences upwind scheme Bruneau and Saad (2006). The CFL condition requires in particular a time step of the order of magnitude of the space step as U is of order one. All the linear terms are treated implicitly and discretized via a second-order centered finite differences scheme. The efficiency of the resolution is obtained by a multigrid procedure using a cell-by-cell relaxation smoother.

So, the results presented in the following sections are obtained by solving directly the above Navier-Stokes equations which do not contain any turbulence modelling.

2.2 Actuators modelling

For the active control, we insert one or several jets in 2D or slots in 3D at the back or on the rear window of the body as shown in Figures 1 or 12. According to its location, the velocity of a given jet is given by $U_j = (u_j, 0, 0)$ or $U_j = (0, 0, u_j)$. It is located at the last solid point of the body before the fluid part of the domain as shown in Figure 2. Each jet has a non dimensional thickness $h_j = 0.024$ and a velocity amplitude A ($u_j = Au_\infty$) corresponding to the forcing intensity $C_\mu = \frac{h_j}{H}\left(\frac{u_j}{u_\infty}\right)^2$. Four amplitudes $A = 0.15$, 0.3, 0.6 and 0.9 which correspond respectively to the forcing intensities $C_\mu = 5 \times 10^{-4}$, 2×10^{-3}, 8×10^{-3} and 1.8×10^{-2} are used.

The penalization method induces to locally modify the divergence-free condition (2) as $\nabla \cdot U = u_j/\delta x$ (see the grey cells in Figure 2), in order the flow does not enter inside the body. The same correction is applied in three dimensions.

2.3 Two- and three-dimensional computations

The first simulations are performed on the domain $\Omega = (0, 15) \times (0, 5)$ in two dimensions (see Figure 3) with a 1920×640 cells uniform mesh. The grid convergence for the same geometry has already been studied in Bruneau et al. (2008) and the grids used here correspond to the finest grid required. The velocity vector is $U = (u, w)$ in two dimensions. The Reynolds number based on the length

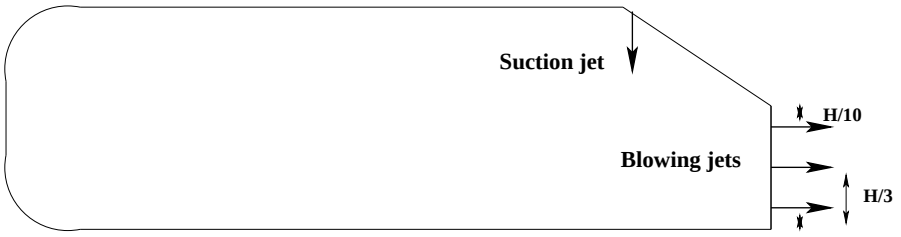

Figure 1 Two-dimensional actuators locations for the active control of the Ahmed body with a rear window (H is the body height).

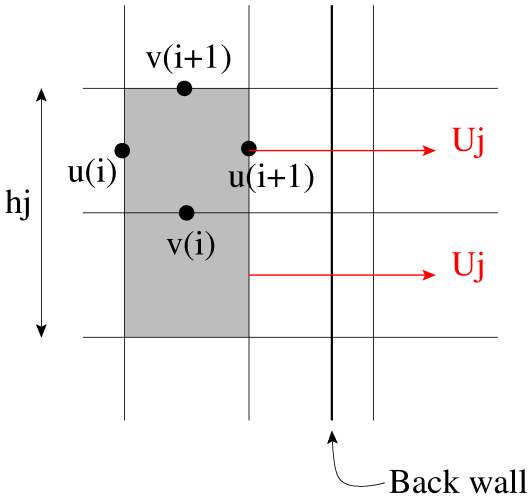

Figure 2 Procedure for active control with a penalization method.

$L = 3.625H$ of the body is $30,000$ that corresponds to $Re = \frac{u_\infty H}{\nu} = 8,275$ where H is the body height and ν the kinematic viscosity of the fluid. This Reynolds number is much lower than real numbers around a vehicle. However this value corresponds to some experiments and is realistic from a numerical point of view as it is possible to get accurate results. Moreover, the flow around the Ahmed body with a rear window on top of a road is dominated by the strong vortices on the rear window and at the back. These features correspond to a wide range of high Reynolds numbers. This paper focuses on the effects of the control on these vortical structures and could be extended to real car dynamics. The mesh step corresponds to $y^+ = \overline{y}\frac{u^+}{\nu} \approx 4$ where $\overline{y}$ and u^+ are respectively, the size of the first cell on the wall and the skin friction velocity. In these computations the space step is then $\delta x = \delta z = 1/128 = 0.0078125$ and the related time step $\delta t = 0.001$. The integration time over which numerical simulations are performed is at least $T = 200$ and the statistics are gathered when the permanent regime is well established over about 3 shedding periods. The mean flows are obtained over at least 50000 snapshots

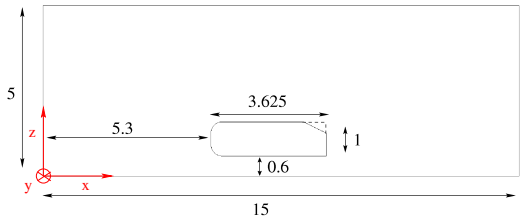

Figure 3 Two-dimensional computational domain around the Ahmed body.

recorded every time step.
In three dimensions the simulations are performed on the domain $\Omega = (0, 12) \times (0, 6) \times (0, 4)$ (see Figure 4) with a $768 \times 384 \times 256$ cells uniform mesh. The velocity vector is $U = (u, v, w)$ in three dimensions. The Reynolds number is the same than in two dimensions and the spanwise dimension is $l = 1.35H$. The

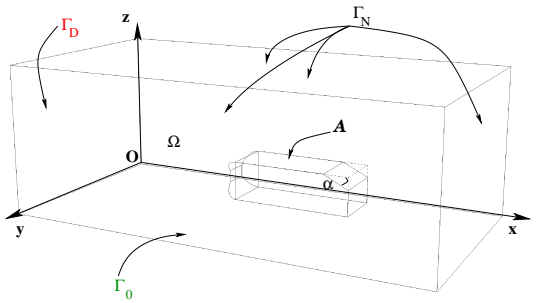

Figure 4 Three-dimensional computational domain around the Ahmed body.

mesh step corresponds now to $y^+ = \overline{y}\frac{u^+}{\nu} \approx 28$. In these computations the space step is then $\delta x = \delta z = 1/64 = 0.015652$ and the related time step $\delta t = 0.002$. The integration time over which the numerical simulations are performed is at least $T = 20$ and the statistics are gathered when the permanent regime is well established over about 3 shedding periods. The mean flows are obtained over at least 7000 snapshots recorded every time step.

2.4 Post-processing variables

As the flow is computed inside the solid body with the penalization method, we can compute the forces by integrating the penalization term U/K on the volume of the body neglecting the time term and the convection term Caltagirone (1994)

$$F_d = \int_{\partial body} \sigma(U,p)\, n\, d\gamma = \int_{body} \nabla \cdot \sigma(U,p)\, dX \approx \int_{body} \frac{U}{K}\, dX.$$

To quantify the effect of the control we shall compare the static pressure coefficient C_p, the total pressure coefficient $C_{p_{st}}$ and the drag coefficient C_d

$$C_p = 2(p - p_0)/U^2 \;\; ; \;\; C_{p_{st}} = 2(p_{st} - p_{st0})/U^2 \;\; ; \;\; C_d = \frac{2F_d}{H}$$

where $p_{st} = p + 1/2U^2$ is the total static pressure and the subscript 0 stands for the inlet quantities. Let us note that the mean value of the static pressure is set to zero at the downstream section of the computational domain.

3 Preliminary results with the two-dimensional geometry

3.1 Flow properties

In Figure 5 the drag coefficient history oscillates around a mean value. The maxima correspond to instantaneous solutions with strong vortices very close to the back wall whereas the minima correspond to instantaneous solutions with low vortical activities in the vicinity of the body back. This can be seen either on the pressure isolines (Figure 6) or on the vorticity (velocity curl) isolines (Figure 7). In these two figures the evolution of the solution during two shedding cycles is plotted. They show in particular the evolution of the vortices in the vicinity of the back. It is visible at time $t = 4.4$ that a strong positive vortex coming from the bottom part of the body induces a strong pressure force at the back wall. When the same vortex is convected downstream (time $t = 5.6$) and that there is no apparition of new vortices, the drag coefficient decreases. Further on, at time $t = 7.6$ there are small vortices in the vicinity of the back that induce very low drag forces at the back wall as there is no pressure well close to the wall. Then the drag coefficient reaches a minimum value more than twice lower than the maximum value.

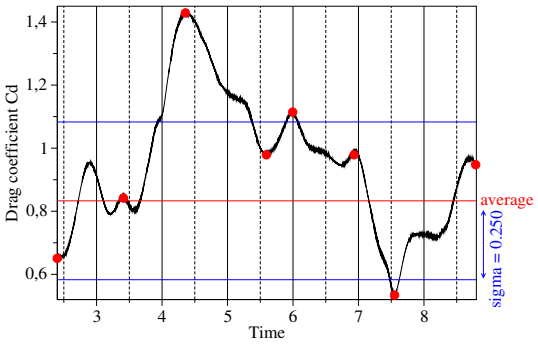

Figure 5 Total drag coefficient (C_d) history during two shedding cycles.

3.2 Control parametric study

As we observed in the previous section, lower values of C_d are achieved when the wake vortex cores are away from the body. So, to take advantage of this property

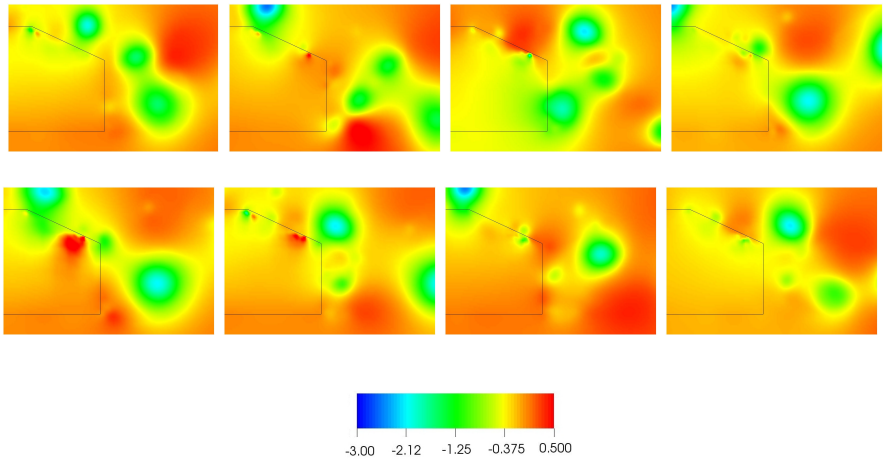

Figure 6 Evolution of the pressure field during two shedding cycles. From top left to bottom right times 2.4, 3.4, 4.4, 5.6, 6, 6.9, 7.6 and 8.8 are plotted.

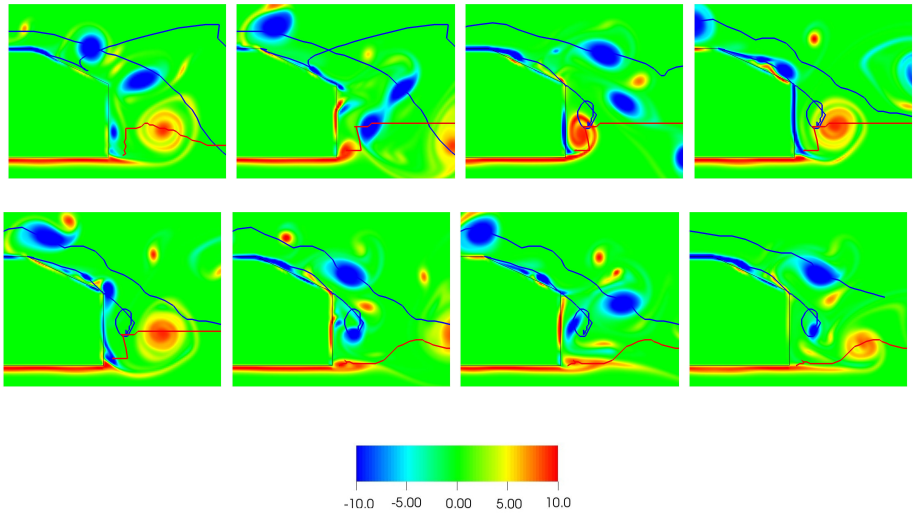

Figure 7 Evolution of the vorticity field during two shedding cycles. From top left to bottom right times 2.4, 3.4, 4.4, 5.6, 6, 6.9, 7.6 and 8.8 are plotted.

an active control with steady blowing jets should put away vortex structures, decreasing the drag forces. The active control is performed putting a suction jet on top of the rear window and one or two blowing jets at the back. Figure 1 shows the three locations selected for the blowing jets in the middle, the upper and the lower part of the square back wall. The upper and lower jets are located at the

distance $H/3$ from the corners. To choose the best amplitude of the steady jet in terms of energy saving, the non dimensional efficiency ξ is used Depeyras (2009)

$$\xi = \frac{P_{saved} - P_{actuator}}{P_{total}} = -\frac{HU_\infty^3 \Delta(C_d)/\eta_{engine} + h_j U_j^3 (K_p + 1/\eta_{actuator})}{HU_\infty^3 C_d/\eta_{engine} + h_j U_j^3 (K_p + 1/\eta_{actuator})} \quad (3)$$

where P denotes the power, the subscript *saved* corresponds to the variation of power with respect to the uncontrolled case, the subscript *actuator* stands for the power related to the actuator only, the subscript *total* indicates that the whole power (body aerodynamics and actuator) is taken into account, $\Delta(C_d)$ is the variation of the drag coefficient, K_p the pressure drop coefficient corresponding to a sudden narrowing followed by a sudden widening (set to 1.34) and η the efficiency of the actuator mechanism or of the engine (set to 30%). If this coefficient is positive, the control is efficient and the greater it is, the more efficient the control is.

To explore the efficiency of this control, we need to study the effect of the jet position and of its amplitude on the body drag coefficient. Taking a steady jet U_j at the middle of the wall, a parametric study on the amplitude is performed. As Table 1 shows the best result is obtained for the highest amplitude as the C_p values on the back and the rear window are increased (Figure 8). However there is no significant efficiency improvement between $A = 0.6$ and $A = 0.9$ (Table 2). Therefore the amplitude $A = 0.6$ will be used for the other tests.

Then the effect of the wall jet location on the drag forces is studied ($A = 0.6$).

Case	$C_{d_{up}}$	Var. $C_{d_{up}}$	$C_{d_{down}}$	Var. $C_{d_{down}}$	C_d	Var. C_d
No control	0.292	-	0.520	-	0.833	-
$U_j = \pm 0.15U_0$	0.275	-6%	0.483	-7%	0.782	-6%
$U_j = \pm 0.3U_0$	0.252	-14%	0.453	-13%	0.729	-12%
$U_j = \pm 0.6U_0$	0.230	-21%	0.429	-18%	0.684	-18%
$U_j = \pm 0.9U_0$	0.210	-28%	0.392	-25%	0.628	-25%

Table 1 Mean drag coefficients for the two-dimensional active control. $C_{d_{up}}$ is the pressure drag coefficient in front of the body and $C_{d_{down}}$ is the pressure drag coefficient on the rear window and on the back of the body. Positive or negative velocities correspond respectively to blowing and suction.

Case	$U_j = 0.15U_0$	$U_j = 0.3U_0$	$U_j = 0.6U_0$	$U_j = 0.9U_0$
ξ	7%	14%	19%	21%

Table 2 Efficiency of the the two-dimensional active control.

As shown in Table 3 the best result is obtained for a jet located on the middle of the body vertical rear part (-18%). Let us note that the active control at the back induces a significant reduction of the pressure drag coefficient both in front

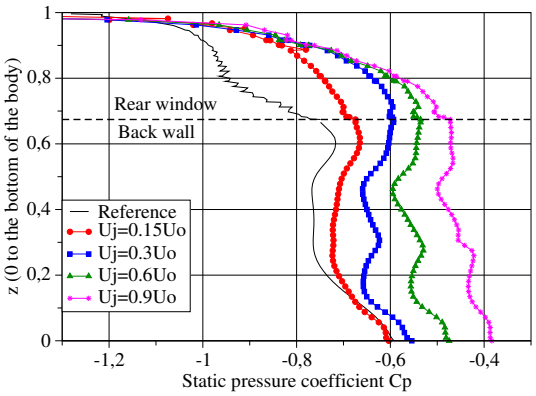

Figure 8 Static pressure coefficient (C_p) profile at the rear end of the body for the two-dimensional active control.

and behind the body. Finally, a double jet configuration with two jets located at a distance $H/3$ from the corners of the back wall is also studied. This control does not improve significantly the drag reduction compared to one jet at the middle.

Case	$C_{d_{up}}$	Var. $C_{d_{up}}$	$C_{d_{down}}$	Var. $C_{d_{down}}$	C_d	Var. C_d
No control	0.292	-	0.520	-	0.833	-
J_{middle}	0.230	-21%	0.429	-17%	0.684	-18%
J_{down}	0.251	-14%	0.466	-10%	0.743	-11%
J_{up}	0.247	-15%	0.443	-15%	0.716	-14%

Table 3 Mean drag coefficients for the two-dimensional active control. $C_{d_{up}}$ is the pressure drag coefficient in front of the body and $C_{d_{down}}$ is the pressure drag coefficient on the rear window and on the back of the body ($A = 0.6$).

4 Active control for the three-dimensional Ahmed body

4.1 Flow properties

With the three-dimensional simulations it is possible to capture all the features of the flow. In particular there are two strong longitudinal vortical structures on both sides of the rear window that contribute significantly to the drag forces. Figure 9 shows clearly how a longitudinal vortex develops on the sharp side of the rear window. The transverse slices on one side of the rear window show the flow rolling up from the corner and growing in the stream wise direction (see Figures 10 and 11).

Moreover the flow is detached on the rear window between these two longitudinal vortices as it can be seen in the left part of Figure 13. Thus there is a recirculation

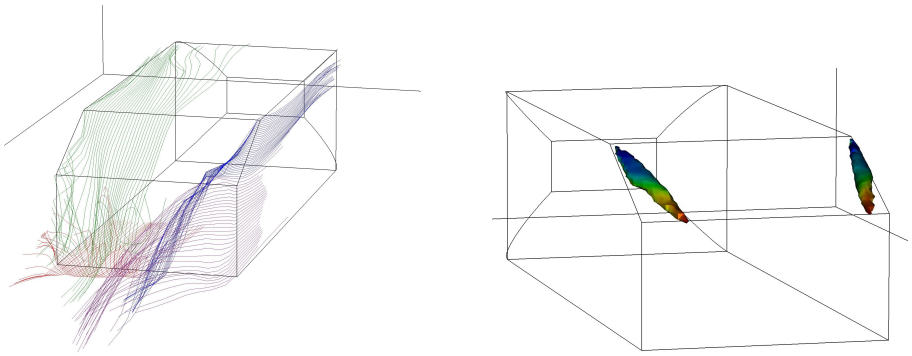

Figure 9 Mean streamlines (left) and Isosurfaces of x-vorticity $\omega_x = -5$ and $\omega_x = 5$ colored by the $C_{p_{st}}$ values (right) in the Ahmed body wake.

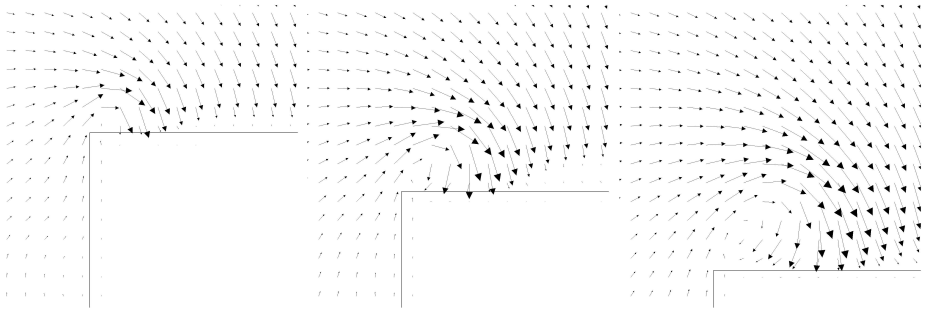

Figure 10 Velocity vectors in the longitudinal vortex for three slices in x on the rear window located at 20%, 50% and 90% of its length.

zone on the rear window that contributes also to the drag forces. This whole flow behaviour can be represented only by three-dimensional simulations.

4.2 Control of the rear window detachment

According to the results of the previous section in two dimensions, the active control is performed with a transverse suction slot on top of the rear window to reduce the detachment and a transverse blowing slot in the middle of the back to push away the vortical structures as shown in Figure 12.

The flow is reattached to the rear window by this control as it is shown by the mean $C_{p_{st}} = 0.8$ isosurface in Figure 13 and by the mean velocity vectors near the left part of the rear window in Figure 14. The mean C_p profile in the median plane in y along the rear window is consequently raised (see the right part of Figure 15). However there is no clear improvement on the back (left part of the same figure). In order to better understand the flow behind the back, the mean streamlines in the median plane in y are plotted in Figure 16. It appears that the mean vortex is splitted into three different vortices whose centers are even closer to the back, which explains the surprising evolution of the mean C_p profile on the

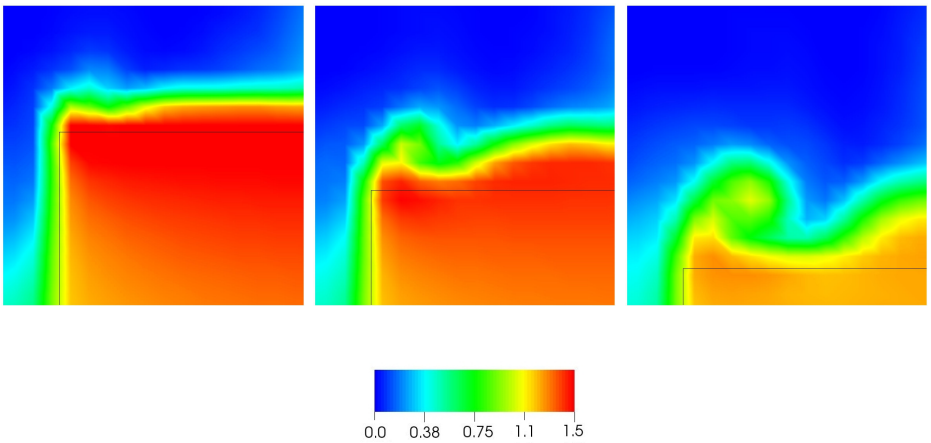

Figure 11 Mean $C_{p_{st}}$ fields for three slices in x on the rear window located at 20%, 50% and 90% of its length.

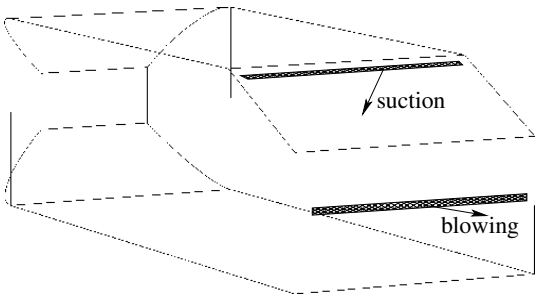

Figure 12 Transverse active control setup.

back. Consequently the resulting drag reduction is lower than expected (see Table 4).

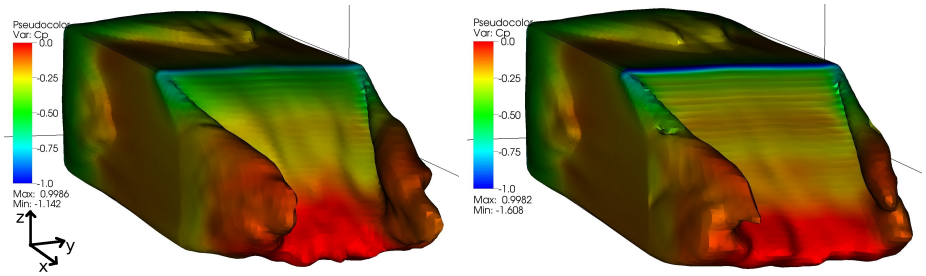

Figure 13 The mean $C_{p_{st}} = 0.8$ isosurface colored by C_p values for the transverse active control, uncontrolled flow (left) and controlled one (right).

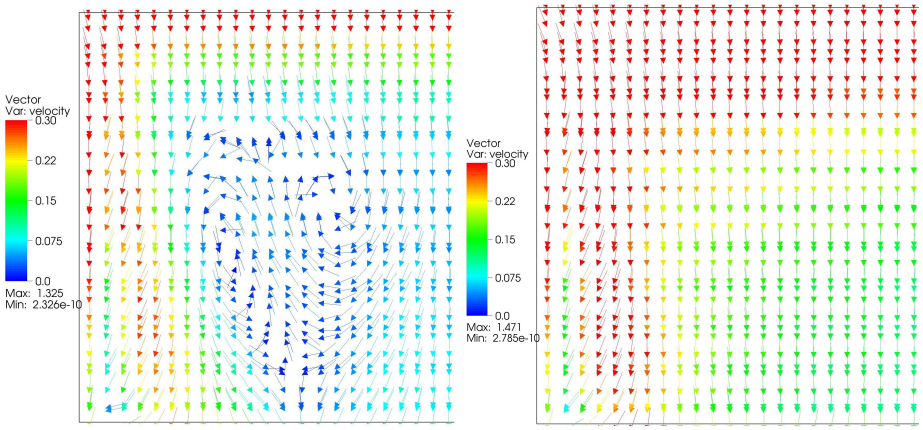

Figure 14 Mean velocity vectors near the left part of the rear window for the transverse active control, uncontrolled flow (left) and controlled one (right).

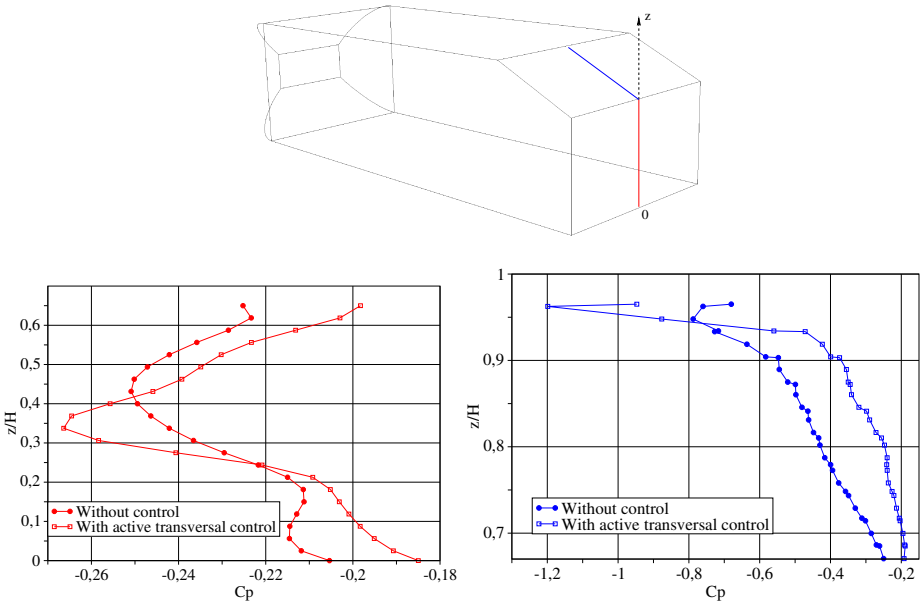

Figure 15 Mean C_p profiles in the median plane in y along the back wall (left) and the rear window (right) for the transverse active control.

4.3 Control of the longitudinal vortices

Another possibility to decrease the drag coefficient is to act on the longitudinal vortices. Keeping the same process we put steady blowing slots on both sides of

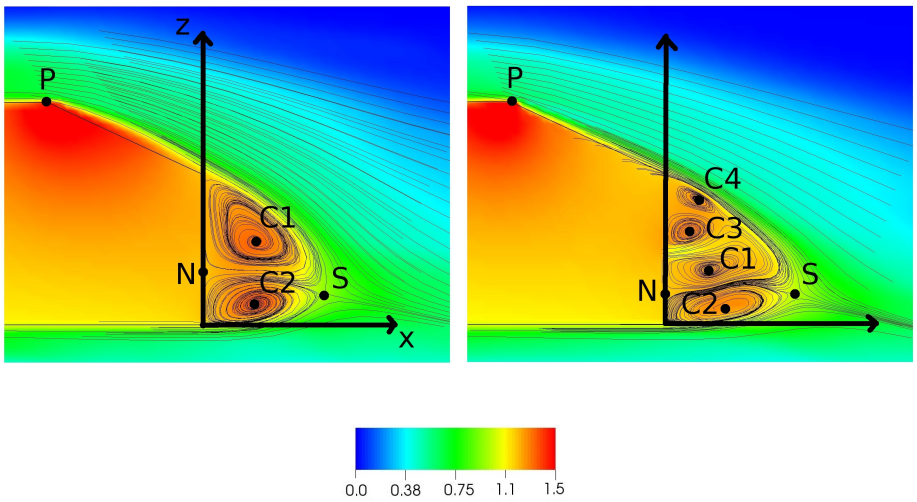

Figure 16 Mean streamlines in the median plane in y colored by the mean C_{pi} values for the transverse active control, uncontrolled flow (left) and controlled one (right).

Case	$C_{d_{up}}$	Var.	$C_{d_{win}}$	Var.	$C_{d_{back}}$	Var.	C_d	Var.
No control	0.177	-	0.149	-	0.130	-	0.371	-
Trans. control	0.176	-1%	0.132	-11%	0.125	4%	0.345	-7%

Table 4 Mean drag coefficients comparison for the transverse active control. $C_{d_{up}}$ is the pressure drag coefficient in front of the body, $C_{d_{win}}$ is the pressure drag coefficient on the rear window and $C_{d_{back}}$ is the pressure drag coefficient on the back of the body.

the rear window as shown in Figure 17. The results show clearly the effect of

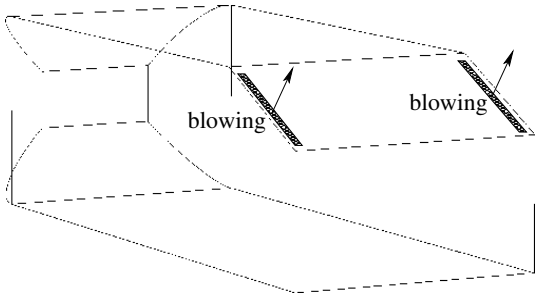

Figure 17 Longitudinal active control configuration.

this active control. The mean C_p is increased not only on the sides but on the whole rear window (see Figure 18). The C_p profile on one side (Figure 19) shows a

drastically increase of the C_p coefficient as the strength of the longitudinal vortices is strongly reduced (Figures 20 and 21). This is clearly shown in Figure 20 where the isosurfaces $\omega_x = |5|$ which are in the middle range of the x-vorticity without control have almost disappeared with the active control. It seems that the effect of this blowing on the rear window sides is to increase the swirl velocity of the side vortices and to push them away diffusing them. A plot of the C_p profile in the

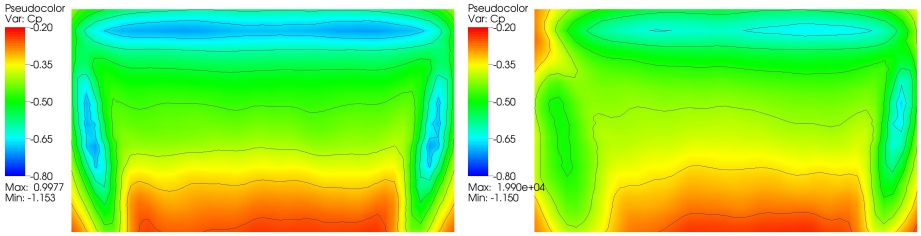

Figure 18 Mean C_p field on the rear window without (left) and with (right) longitudinal active control.

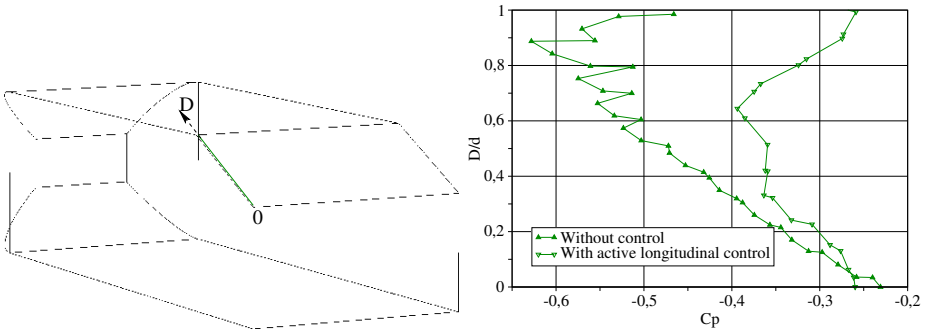

Figure 19 Mean C_p profile on the edge of the window for the longitudinal active control.

median plane in y along the back wall and the rear window shows that the C_p is increased on the rear window and in the top of the back wall. On the contrary it is decreased on the bottom of the back wall (Figure 22). Nevertheless this control of the longitudinal vortices is very efficient thanks to the high drag decrease on the rear window (17%) as a 11% reduction of the global drag coefficient is achieved (Table 5).

4.4 Coupling of the transverse and longitudinal controls

At last, to take benefit of the two previous controls, a coupling procedure of both transverse and longitudinal controls is implemented (Figure 23). The aim is to keep the reattachement on the rear window obtained by suction, to decrease the

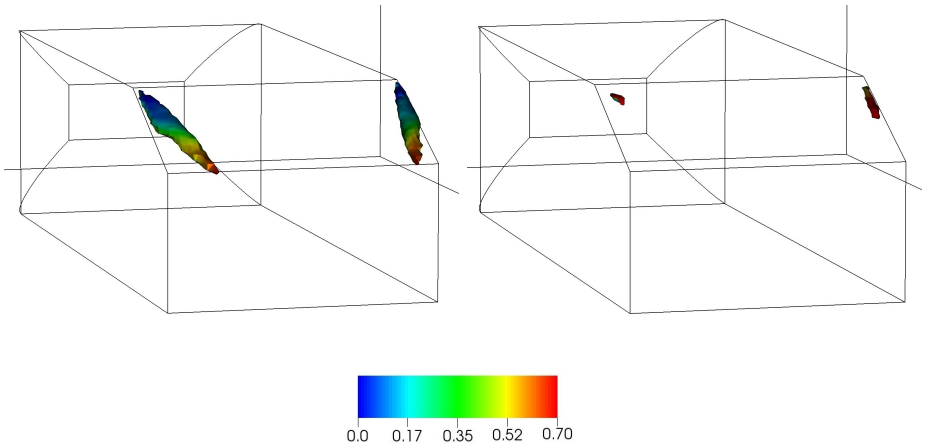

Figure 20 Mean x-vorticity isosurfaces $\omega_x = -5$ and $\omega_x = 5$ colored by the mean C_{pi} values without (left) and with (right) longitudinal active control.

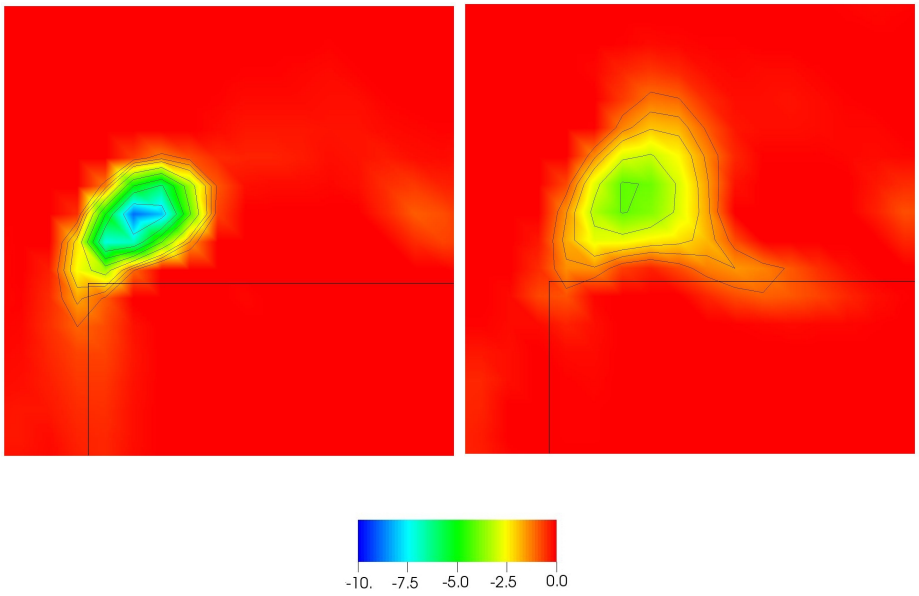

Figure 21 Mean x-vorticity field for the slice in x in the middle of the rear window without (left) and with (right) longitudinal active control.

influence of the longitudinal vortices and to increase the C_p at the back. The effect of this control on the vehicle front part is identical to the transverse control due to the suction (see Table 6). On the contrary the reduction of the drag coefficient on the rear window is improved as the two beneficial effects are added. Moreover, as the effect of the blowing at the back is positive at the bottom part, the total drag coefficient reaches a 13% reduction. This result is confirmed by the C_p profile

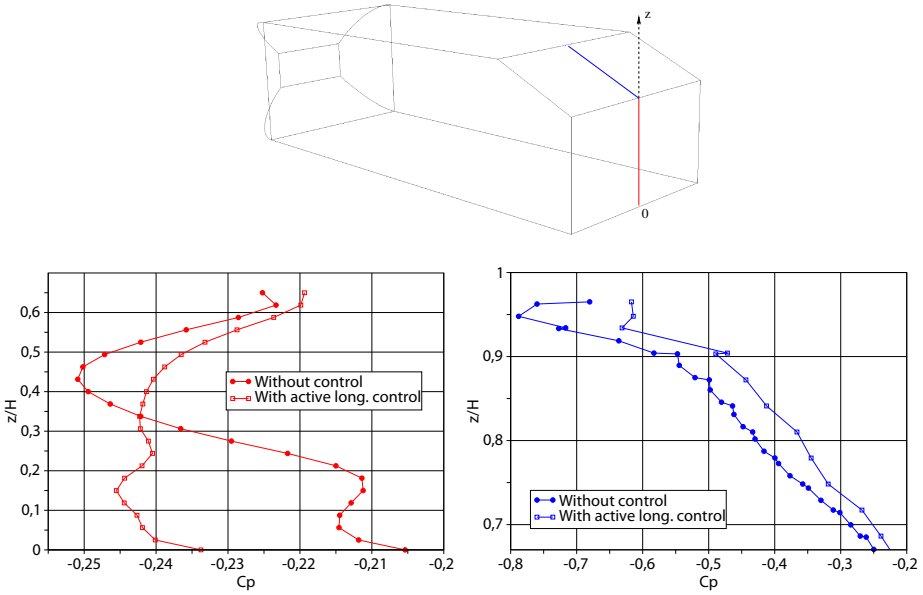

Figure 22 Mean C_p profile in the median plane in y along the back wall (left) and the rear window (right) for the longitudinal active control.

Case	$C_{d_{up}}$	Var.	$C_{d_{win}}$	Var.	$C_{d_{back}}$	Var.	C_d	Var.
No control	0.177	-	0.149	-	0.130	-	0.371	-
Longi. control	0.164	-7%	0.123	-17%	0.130	-	0.332	-11%

Table 5 Mean drag coefficients comparison for the longitudinal active control. $C_{d_{up}}$ is the pressure drag coefficient in front of the body, $C_{d_{win}}$ is the pressure drag coefficient on the rear window and $C_{d_{back}}$ is the pressure drag coefficient on the back of the body.

in Figure 24 as the profile in the bottom part rises from a mean value of -0.24 to a much higher mean value of -0.19. That corresponds to a 20% increase.

5 Conclusions

In this paper, steady active control techniques are studied in order to reduce the drag forces around the two-dimensional and three-dimensional Ahmed body with a 25° rear window. A parametric study for the two-dimensional case is performed to find out the best location and amplitude of the control jets. Numerical simulations of the three-dimensional flow capture the main vortical structures that are responsible for the drag forces on the body. In order to reduce the drag coefficient, suction or blowing slots are implemented on some appropriate locations

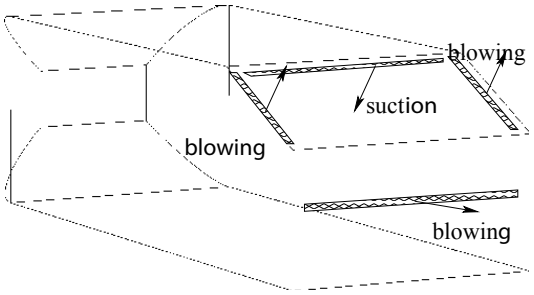

Figure 23 Coupled active control configuration.

Case	$C_{d_{up}}$	Var.	$C_{d_{win}}$	Var.	$C_{d_{back}}$	Var.	C_d	Var.
No control	0.177	-	0.149	-	0.130	-	0.371	-
Trans. control	0.176	-1%	0.132	-11%	0.125	-4%	0.345	-7%
Longi. control	0.164	-7%	0.123	-17%	0.130	-	0.332	-11%
Coupling	0.176	-1%	0.118	-21%	0.128	-2%	0.323	-13%

Table 6 Mean drag coefficients comparison for the various active controls. $C_{d_{up}}$ is the pressure drag coefficient in front of the body, $C_{d_{win}}$ is the pressure drag coefficient on the rear window and $C_{d_{back}}$ is the pressure drag coefficient on the back of the body.

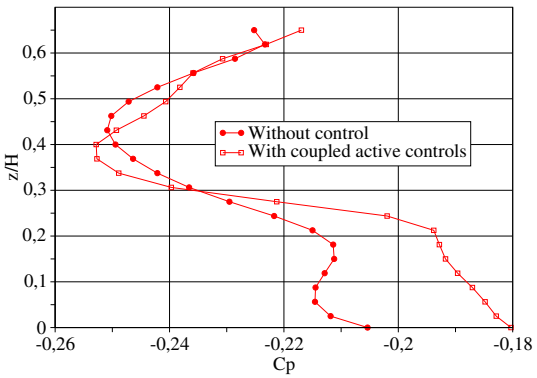

Figure 24 Mean C_p profile in the median plane in y along the back wall for the coupled active controls.

in the rear part of the body. Three actions are proposed: a transverse suction on the top of the rear window reattaches the flow, a transverse blowing at the back wall breaks down the large recirculation areas behind the body and a blowing on both sides of the rear window weakens the longitudinal vortices. The action on the

longitudinal vortices gives the best drag reduction among the three and a coupling of these three actions allows to reach a 13% reduction of the drag coefficient.

References

Ahmed S. R., Ramm G. and Faltin G. (1984) 'Some Salient Features of the Time - Averaged Ground Vehicle Wake', *SAE-Paper*, 840300.

Angot P., Bruneau C.-H. and Fabrie P. (1999) 'A penalization method to take into account obstacles in incompressible viscous flows', *Numerische Mathematik*, Vol. 81, pp.497–520.

Bruneau C.-H. and Fabrie P. (1994) 'Effective downstream boundary conditions for incompressible Navier-Stokes equations', *Int. J. Num. Meth. Fluids*, Vol. 19, pp.693-705.

Bruneau C.-H. and Mortazavi I. (2008) 'Numerical modelling and passive flow control using porous media', *Computers & Fluids*, Vol. 37, n^0 5.

Bruneau C.-H., Mortazavi I. and Gilliéron P. (2008) 'Passive control around the two-dimensional square back Ahmed body using porous devices', *J. Fluids Eng.*, Vol. 130, pp.1-33.

Bruneau C.-H. and Saad M. (2006) 'The 2D lid-driven cavity problem revisited', *Comp. & Fluids* Vol. 35, pp.326-348.

Brunn A., Wassen E., Sperber D., Nitsche W. and Thiele F. (2007) 'Active Drag Control for a Generic Car Model', *King (ed.) Active Flow Control, Notes on Numerical Fluid Mechanics and Multidisciplinary Design*, Vol. 95, pp.247-259.

Caltagirone J.-P. (1994) 'Sur l'intéraction fluide-milieu poreux: Application au calcul d'efforts exercés sur un obstacle par un fluide visqueux', *CRAS*, Vol. 318, pp.571-577.

Cooper K.R. (1985) 'The effect of front-edge rounding and rear-edge shapping on the aerodynamic drag of bluff vehicles in ground proximity', *SAE Paper* 850288.

Depeyras D. (2009) 'Contrôles actifs et passifs appliqués à l'aérodynamique automobile', Ph D thesis, Bordeaux, France.

Fieldler H.E. and Fernholz H.H. (1990) 'On the management and control of turbulent shear flows, *Prog. Aero. Sci.* 27.

Gilliéron P. (2002) 'Contrôle des écoulements appliqué à l'automobile. Etat de l'art', *Meca. Ind.*, Elsevier.

Gilliéron P. and Chometon F. (1999) 'Modelling of Stationary Three-Dimensional Separated Air Flows around an Ahmed Reference Model', *ESAIM*, Vol. 7.

Gilliéron P. and Spohn A. (2002) 'Flow Separations Generated by a Simplified Geometry of an Automotive Vehicle', *IUTAM Symp. Unsteady Separated Flows.*

Krajnović S. and Davidson L. (2003) 'Numerical study of the flow around the bus-shaped body', *ASME J. Fluids Eng.*, Vol. 125.

Lienhart H., Stoots C. and Becker S. (2000) 'Flow and turbulence structures in the wake of a simplified car model (Ahmed model)', *DGLR Fach Symp. Der AG STAB.*

Onorato M., Costelli A.F. and Garonne A. (1984) 'Drag measurement through wake analysis', *SAE Paper*, Vol. 569.

Roshko A. and Koening K. (1976) 'Interaction effects on the drag of bluff bodies in tandem, Symposium on Aerodynamic Drag Mechanisms of Bluff Bodies and Road Vehicles', *General Motors Report.*

Rouméas M., Gilliéron P. and Kourta A. (2009) 'Analysis and control of the near-wake flow over a square-back geometry', *Computers & Fluids*, Vol. 38, pp.60-70.